quantum beam
science

Article

Multi-Scale Microstructure Investigation for a $PM_{2.5}$ Air-Filter Efficiency Study of Non-Woven Polypropylene

Tu-Ngoc Lam [1,2], Chen-Hsien Wu [3], Sheng-Hsiu Huang [4], Wen-Ching Ko [1,3], Yu-Lih Huang [1], Chia-Yin Ma [1], Chun-Chieh Wang [5,*] and E-Wen Huang [1,*]

[1] Department of Materials Science and Engineering, National Chiao Tung University, 1001 University Road, Hsinchu 30010, Taiwan
[2] Department of Physics, College of Education, Can Tho University, Can Tho City 900100, Vietnam
[3] Institute of Applied Mechanics, National Taiwan University, 1, Sec. 4, Roosevelt Road, Taipei 10617, Taiwan
[4] Institute of Occupational Medicine and Industrial Hygiene, National Taiwan University, No. 17, Xu-Zhou Rd., Taipei 10055, Taiwan
[5] National Synchrotron Radiation Research Center, Hsinchu 30076, Taiwan
* Correspondence: wang.jay@nsrrc.org.tw (C.-C.W.); ewenhuang@nctu.edu.tw (E.W.H.)

Received: 29 August 2019; Accepted: 24 October 2019; Published: 28 October 2019

Abstract: A N95 face-piece respirator and a 3M air filter composed of non-woven polypropylene filter material were investigated for their multi-scale microstructure and resulting filtration performance. Filtration mechanisms of each system are found and quantified. Both media showed a gradually decrease of the most penetrating particle size with respect to an increase in face velocity or surface charge density. Increasing the face velocity and porosity dramatically degraded the collection efficiency in the 3M filter rather than in the N95 system. We exploited three-dimensional X-ray tomography to characterize the morphological and geometrical properties of the fiber arrangement and deposition of aerosol on the fiber surface. Tuning the most predominant material parameters to achieve a precedence in lower pressure drop or higher collection efficiency in a specifically captured particle size range is of great requisite to a peculiar application of the filter media.

Keywords: fibrous filter; electret filter; aerosol; porosity; X-ray tomography

1. Introduction

Modern technology has improved the quality of life in many aspects, however, the other side of such a rapid development of industry is severe air pollution, causing serious human health hazards due to the deep penetration of particular matter with fine particle sizes below 2.5 µm ($PM_{2.5}$) into human lungs [1–3]. Air filtration is one of the most urgent and prioritized tasks for the protection of the global environment and human health by removing aerosol particles through air filter media. Air filter media is commonly made from fibrous filters comprising randomly arranged fibers whose distances are larger than the sizes of aerosol particles [4]. Fibrous filters basically capture aerosol particles via four physical mechanisms, including gravity settling, inertia impact, interception, and Brownian diffusion in which each of them plays a crucial role for a particular size range of aerosol particles [4,5]. The particle size at the lowest filtration efficiency, named as the most penetrating particle size (MPPS), typically around 0.3 µm or smaller, is used to determine the dominant capture mechanism of the air filter [3,4,6]. An ideal filter media is expected to perform both high filtration efficiency and low pressure drop that is hard to acquire from traditional fibrous filters. To satisfy high collection efficiency of fibrous filters for further applications, electret filters have been widely applied in the manufacture of commercial air filter media. Electret filters are dielectric materials-based fibrous filters that possess quasi-permanent static electric charge on the fiber surfaces [7] in which the electrostatic force dramatically enhances filtration efficiency and is responsible for the main capture of fine aerosol particles, resulting in a significant shift towards a smaller particle size of MPPS [8–11].

One of the most serious challenges of general air filter media is a tradeoff between collection efficiency and pressure drop because the fibers collect aerosol particles and affect the drag force on the gas stream simultaneously [4]. Those two important factors of the electret filters involve a variety of parameters such as the microstructural characteristics of fibrous material (fiber diameter, thickness, porosity, fiber arrangement), surface charge density, and environmental conditions (face velocity, aerosol particle diameter, temperature, humidity). In spite of using the same fibrous material, its own microstructure is possibly tuned to optimize either high collection efficiency or low pressure drop for a specific application of the air filter media that can be engineered through the fabrication process. There are two major application types of the air filter media, wearable respirators and air filter equipment (vacuum cleaner bags, indoor air cleaning, indoor air purifiers), possessing different priority criteria of fibrous properties. To unravel the behavior of structural properties to collection efficiencies and to acquire comparable results from theoretical predictions and experimental data, considerable effort has been devoted to the development of filtration modeling using three-dimensional (3D) filter structures obtained by different approaches as more and more microstructural properties of filter media have been taken into account [12–15]. Moreover, the filtration performance is strongly influenced by the porosity of the fibrous material but no reliable methods in determining porosity is well known.

In this study, we have attempted to specify the porosity through different kinds of methods including theoretical analysis, gravimetric measurement, GrabCut analysis from scanning electron microscope (SEM) images, and 3D tomography analysis from transmission X-ray microscopy (TXM). The 3D TXM tomography was especially utilized to provide useful morphological and geometrical properties of solid or hollow fibers, fiber arrangement, fiber entanglement, and fiber-particle contact for two majorly different non-woven polypropylene (PP)-based $PM_{2.5}$ air filter media, namely the N95 respirator and the 3M filter used in air purifiers. Furthermore, the filtration performances of these two media were experimentally investigated and compared with the theoretical results in order to elucidate the major characterization parameters of microstructural fibers in governing the dominant filtration mechanism of N95 respirators and 3M filters in the presence and absence of electrostatic attraction. Understanding the impact of fiber characterization on filtration performance plays a vital role in the design of efficient fibrous filters for distinct application purposes.

2. Materials and Methods

2.1. Specimen Preparation

Two distinct commercial air filter media, the N95 face-piece respirator 8210 Plus® and the 3M filter 9809-R® used in air purifiers were chosen in this work because they are widely used and have a great market share. Both electret filter media are composed of melt-blown non-woven PP material. The N95 respirator, a disposable dust mask, is worn to protect people from hazardous substances. It consists of three layers of which the middle one acts as a filter layer, the outer and inner are support and comfort layers, respectively. The 3M air filter has only one filter layer. The N95 mask should not be worn for more than 8 h while the 3M filter can be used up to 2000 h. The different use times of the N95 mask and the 3M filter will be extensively clarified and associated with their collection efficiency and pressure drop.

2.2. Filtration Test System

The two filters were tested as origin specimens. Moreover, we modified these two systems by dipping them in isopropanol (IPA) for 5 min and then drying them naturally to remove the surface charge density [5,8,16] for studying the impact of electrostatic charges on collection efficiency. All the filtration tests were performed at ambient temperate and humidity. Sodium chloride (NaCl) monodisperse aerosols in the particle size range of 10 to 750 nm were used as the emission source of particles. Experimental filtration performances were compared with the filtration efficiencies of single fiber theory to clarify the main capture mechanism of the two filter media.

2.3. Grabcut Analysis

SEM images were processed by the GrabCut image segmentation algorithm [17] to analyze the surface topography of the fibers. The image was pre-processed by the GrabCut method; firstly to define the fiber boundary and the energy function, and then to employ the algorithm for separating the image into foreground and background segmentation; thus, the surface morphology of the initially processed surface was obtained. Based on the calculation and porosity analysis method of Martin III et al. [18], the concept of representative elemental area (REA) was utilized to calculate the convergence value of the porosity by calculating a plurality of pore distribution. The value of average porosity is defined within the maximum of porosity curve region and within ±5% of the minimum region.

2.4. 3D Tomography

Transmission X-ray microscopy is a non-destructive image microscopy technique which allows 3D tomography analysis of fiber reconstruction in fibrous materials. TXM tomography was carried out at beamline (BL) 01B1, National Synchrotron Radiation Research Center (NSRRC) in Taiwan with the wavelength of 1.54 Å (8 keV) and spatial resolution of 60 nm. The protocol is archived [19,20]. TXM can construct 3D geometric configuration of materials by capturing a series of 2D X-ray radiographies from different viewing angles. After the auto-alignment processing using the Faproma image registration algorithm [21,22] and filtered back-projection (FBP) reconstruction algorithm, the radiographies can be reconstructed to a 3D tomography. Amira software is then applied to classify, segment the size, shape, or other measurable parameters in the post-processing analysis of the 3D reconstructed tomography, and to filter them into different categories for extracting the structure of interest. The 3D tomography of fiber reconstruction provides useful microstructure characterization not only on the geometrical arrangement of fiber–fiber, fiber–particle but also on the porosity distribution of the two filter media. More detail information of TXM can be found elsewhere [23].

3. Results

3.1. Filter Morphology Characterization

The surface morphologies of the N95 mask and 3M filter before capturing NaCl particles were obtained by SEM images at the same magnification. Fibers with different sizes were randomly arranged, shown in Figure 1a,b. In Figure 1c,d, the capture of different sizes of NaCl aerosols on the fiber surfaces was clearly observed. However, in order to clarify a particular distribution of fibers and NaCl particles, we employed ImageJ software to perform subsequent image processing and analysis from the SEM images. Figure 1e,f display the fiber distribution in which the average fiber diameters in the N95 and 3M filter media were 2.9 and 24.6 μm, respectively. The average fiber diameter of the 3M filter was eight times bigger and the fiber diameter distribution in the 3M filter was more homogeneous than that in the N95 mask. Our SEM results were found to agree well with the fiber diameter distribution provided in the Patent [24–26]. As we can observe in Figure 1g,h, NaCl aerosols with smaller sizes were preferably collected by the N95 mask rather than by the 3M filter, in which the highest proportion was detected at the favorably captured NaCl particle sizes of 460 and 590 nm in the N95 mask and the 3M filter, respectively. In addition, the thicknesses of the N95 and 3M filters were measured by immersing them in liquid nitrogen following the direct freeze fracture pretreatment and taken by cross-section SEM, found to be 1.53 and 1.23 mm, respectively.

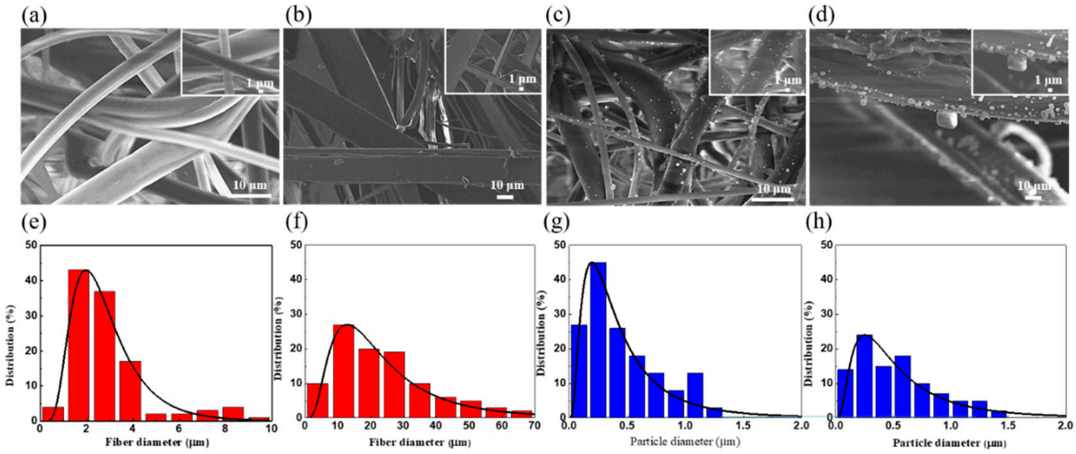

Figure 1. SEM images of (**a**) N95 mask and (**b**) 3M filter before capturing NaCl; those of (**c**) N95 mask and (**d**) 3M filter after capturing NaCl aerosols. Fiber distribution in (**e**) N95 mask and (**f**) 3M filter. The distribution of NaCl aerosols in (**g**) N95 mask and (**h**) 3M filter.

3.2. Filter Performance

The various PP material-based applications depend on filter performance. Figure 2a depicts the collection efficiency of the N95 mask and the 3M filter as a function of face velocity. All the collection efficiencies showed the typical curve shape in which the minimum removal efficiency is obtained at MPPS. The collection efficiency of the N95 mask was around 97%, which revealed a more pronounced efficiency compared to 45% by the 3M filter. Furthermore, the collection efficiencies gradually increased with decreasing face velocity for both the N95 and 3M filters, which are similar to the results obtained in previous studies [3,27,28]. The filtration efficiencies at MPPS in the N95 mask were 97.52% (53 nm), 96.37% (53 nm), and 93.81 % (43 nm) and those in the 3M filter were 49.89% (346 nm), 41% (300 nm), and 35.93% (202 nm) at the face velocity of 5, 10, and 15 cm/s, respectively. The particle sizes around 50 and 300 nm were the most penetrating for the filtration process in the N95 mask and the 3M filter, respectively. An increase of face velocity results in an obvious trend of MPPS shifting towards a lower value, in agreement with previous reports [29].

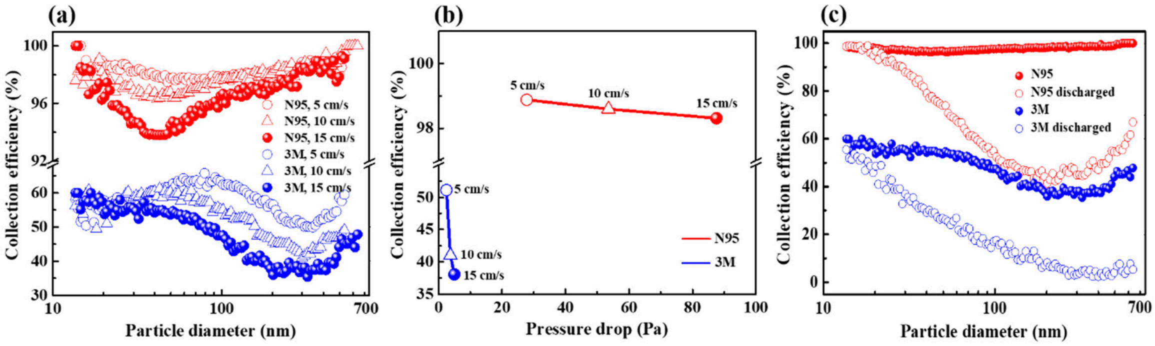

Figure 2. (**a**) Collection efficiency of the N95 and 3M filters at different face velocities. (**b**) Collection efficiency versus pressure drop of the N95 and 3M filters as a function of face velocity. (**c**) Collection efficiency of the N95 and 3M filters before and after treatment with IPA.

The effect of face velocity on the pressure drop is described in Figure 2b. Compared with the variation of collection efficiency, the change of pressure drop indicates an opposite tendency in which the pressure drop decreased linearly with decreasing face velocity for both the N95 and 3M filters. Decreasing the face velocity had a more significantly positive impact on the collection efficiency for the 3M filter while on the pressure drop for the N95 mask. It implies that the collection efficiency is the priority factor in the N95 mask while the pressure drop is the preferable element in the 3M filter. This result allows a definitely appropriate explanation for the use times of the two filter media. The low face velocity has a positive effect on both collection efficiency and pressure drop and it is one of the tunable parameters in enhancing filter performance due to the shorter interaction time between particles and fibers [5,30]. However, low face velocity is not feasible for practical applications of the filter media as a face-piece respiratory protector. The optimal face velocity of 10 cm/s is commonly used for the filtration performance test to attain a good balance between collection efficiency and pressure drop and it was also chosen for further filtration tests, as follows.

Based on the measured MPPS, the dominant capture mechanisms for the N95 mask were predicted to be diffusional deposition and electrostatic attraction while the major ones for the 3M filter were forecasted to be diffusion, interception, and electrostatic attraction. To further investigate the role of electrostatic attraction in filter performance, the two media treated with IPA (discharged specimens) were compared with the original ones. In Figure 2c, the two originally charged filters performed at a much higher collection efficiency, with a shift of MPPS towards lower values, as compared with the discharged filters, which agrees with previous works [8,9]. The filtration efficiencies of the N95 and 3M charged filters were two and twelve times higher than those of the N95 and 3M discharged ones, respectively. The absence of electrostatic force leads to the shift of MPPS from 200 to 53 nm and from 400 to 300 nm in the N95 and 3M filters, respectively. The results demonstrate that the electrostatic filters are of great important in capturing fine aerosol particles with extremely high filtration efficiency.

3.3. Filtration Mechanism

The four main mechanisms of aerosol filtration were determined based on theoretical single fiber efficiency and the theoretical analyses were compared with the experimental results to examine the dominant filtration mechanism. The microscopic property of single fiber efficiency E_Σ is the sum of four individual collection efficiencies, including interception E_R [31], impaction E_I [31], diffusion E_D [31], and electrostatic E_E [32], shown as

$$E_\Sigma = E_R + E_I + E_D + E_E \tag{1}$$

The macroscopic property of collection efficiency [33] is defined as

$$E = 1 - \exp\left(\frac{-4\alpha E_\Sigma t}{\pi d_f}\right) \tag{2}$$

in which α is the solidity or packing density of the filter, $\alpha = 1 - \text{porosity}$, t is the filter thickness, and d_f is the fiber diameter.

Figure 3 makes a comparison between the theoretical analysis and experimental observation of filtration efficiencies for the N95 and 3M filters. The theoretical single fiber efficiencies were plotted for the N95 and 3M owning fiber diameters of 2.88 and 24.61 μm, solidities of 0.083 and 0.037 (derived from the gravimetric measurement shown in the next section), respectively. The face velocity was 10 cm/s. Among individual mechanisms, the diffusion deposition is more predominant in capturing smaller particle sizes below 100 nm while the electrostatic attraction discloses a key role in capturing a wider range of aerosol sizes with extremely high collection efficiency. The theoretically total efficiency with the presence of electrostatic ($\mathrm{E_{w\ E}}$-theo) exhibits a striking enhancement of filtration efficiency in the size distribution of fine particles compared to that without the presence of electrostatic ($\mathrm{E_{w/o\ E}}$-theo), which entirely agrees with the experimentally total efficiency with and without the presence of electrostatic ($\mathrm{E_{w\ E}}$-exp and $\mathrm{E_{w/o\ E}}$-exp, respectively). Similarly measured and predicted collection efficiency curves were achieved in the N95 mask rather than in the 3M filter, which is explained in the following part.

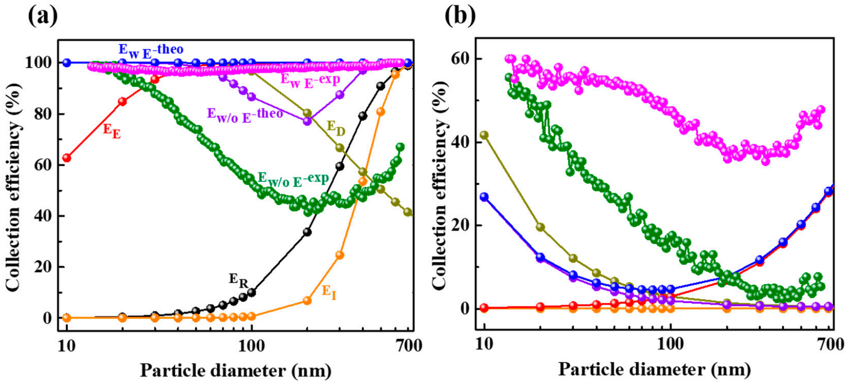

Figure 3. Interception, impaction, diffusion, electrostatic, theoretical single fiber efficiencies, and experimental collection efficiencies with and without the presence of electrostatic for the N95 (**a**) and 3M (**b**) filters.

3.4. Dependence of Filter Performance on Porosity

The collection efficiency is greatly influenced by electrostatic force while both collection efficiency and pressure drop are strongly governed by the porosity of the fibrous filters. We herein explored the dependence of collection efficiency and pressure drop on porosity based on the theoretical analysis which derives from the experimentally measured average fiber diameter at the face velocity of 10 cm/s. Since the fiber sizes of the N95 and 3M filters were larger than 1 μm, we can use the equation below to calculate the pressure drop Δp [33].

$$\Delta p = \frac{\eta t U_0 f(\alpha)}{d_f^2} \tag{3}$$

where η is the air viscosity, U_o is the face velocity, $f(\alpha)$ is the theoretical fiber bulk density, and $f(\alpha) = 64\alpha^{1.5}\left(1 + 56\alpha^3\right)$ for $0.006 < \alpha < 0.3$ (or 70% < porosity < 99.4%).

Figure 4 describes the pressure drop and collection efficiency variation as a function of porosity which was assumed in the range of 70% to 99.4%. Both the pressure drop and collection efficiency decreased with increasing porosity. However, the pressure drop of the N95 mask suffers a much more pronounced decline than the 3M filter while the collection efficiency of the 3M filter endures a more serious reduction than the N95 mask. It can be suggested that an optimal porosity of 95% in the N95 mask and that of 70% in the 3M filter enable a fairly high filtration efficiency with a relatively low pressure drop. This optimized porosity of the N95 mask approximates to the porosity used in the theoretical single fiber efficiency, which was supposed to have caused a small discrepancy between the measured and predicted collection efficiency curves in Figure 3a. On the contrary, a considerable disparity between the optimal porosity and the porosity used in the theoretical single fiber efficiency of the 3M filter was attributed to a large difference between the measured and predicted collection efficiency curves in Figure 3b.

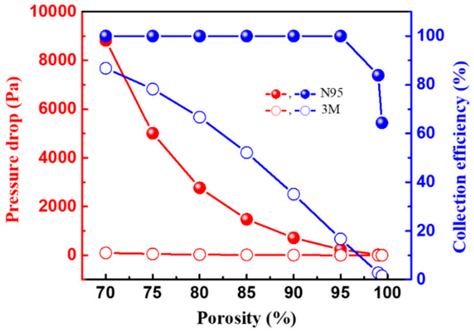

Figure 4. Theoretical analysis of collection efficiency and pressure drop of the N95 and 3M filters as a function of filter porosity.

4. Discussion

Since porosity of the fibrous filter is one of the most crucial parameters strongly affecting both collection efficiency and pressure drop, we experimentally specify the porosity based on GrabCut analysis from SEM images and 3D tomography analysis from TXM in comparison with reference values obtained from theoretical analysis and gravimetric measurement. Based on Equation (3), we calculated the porosity from the experimentally measured pressure drop at the face velocity of 10 cm/s. The porosity values of the N95 and 3M filters were 98.1% and 93.7%, respectively.

Another method to identify porosity is the gravimetric measurement in which porosity is defined as

$$\text{Porosity} = 1 - \frac{\rho_{\text{filter}}}{\rho_{\text{PP}}} \tag{4}$$

where ρ_{filter} is the density of the filter and ρ_{PP} is the density of PP material. The porosity values of the N95 and 3M filters based on the gravimetric measurement were determined to be 91.7% and 96.3%, respectively.

The porosity can also be obtained based on imaging processing and analysis. We employed the GrabCut analysis from SEM images in which the porosity values of the N95 and 3M filters were found to be 78% and 96%, respectively, shown in Figure 5.

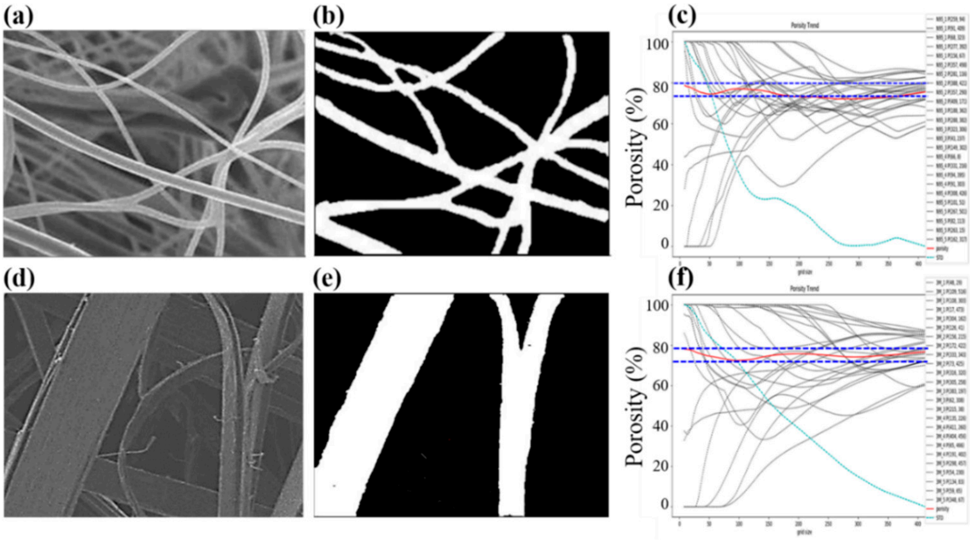

Figure 5. The original SEM image, GrabCut processed image, and REA result of the N95 mask in (**a**), (**b**), and (**c**); those of the 3M filter in (**d**), (**e**), and (**f**), respectively.

In addition, we attempted to determine the filter porosity which was calculated by the volume of the selected fiber over the total volume of the 3D TXM images reconstructed using Amira software analysis, seen in Figure 6a,c.

$$\text{Porosity} = 1 - \frac{\text{Fiber volume}}{\text{Total volume}} \tag{5}$$

The 3D tomography analysis-based porosity values of the N95 and 3M filters were averaged from three different measured areas of 15 x 15 μm, found to be 83.5% and 88.7%, respectively.

The porosity values obtained by theoretical analysis and gravimetric measurement are indeed in the same order and exhibit negligible discrepancies. The porosity obtained by GrabCut analysis from SEM images discloses the largest error value, which is attributed to the observation of only surface morphology of the samples. Taking the internal microstructure of filters into account, the porosity values obtained by 3D TXM are closer to those calculated by theoretical analysis and gravimetric method. Such a small difference is ascribed to a limited number of mapping areas. It can be suggested that the more expanded the area mapped by 3D TXM tomography is, the more accurate the porosity value is.

Therefore, the 3D tomography analysis from TXM may be considered as a promisingly alternative approach to determine the porosity of fibrous filters. In addition, although much attention has been given to theoretical filtration models of aligned arrangements of fiber networks, further analyses of complicated fibrous networks such as fiber–fiber contact interactions, fiber–particle direct attachments, fiber orientation, fiber morphology, fiber diameter, diameter distribution, and porosity should be fully taken into consideration and much more effort is needed to completely elucidate the significant role of fibrous networks in governing the dominant capture mechanism of the filters. Such intricate fibrous networks may be gained through the reconstruction of 3D TXM images which clearly enables a visualization of geometrical arrangement of fiber entanglement positions at different viewing angles. Furthermore, the reconstruction images along the *z*-axis allows the identification of structural morphology properties in which N95 and 3M fibrous filters were characterized to be solid fibers due to an unobservable inner boundary, as shown in Figure 6b,d, respectively. We conducted 3D TXM tomography of the N95 and 3M filters after capturing NaCl; however, the direct attachments between fibers and particles cannot be clearly distinguished with the naked eye, as expected. Because there is not much difference in the absorption coefficients between the PP material and NaCl, the image contrast is not good enough for further image processing. Further efforts to attain a better contrast between fiber materials and aerosols are necessary since the directly adhesive contact behaviors of aerosols deposited on the fiber surfaces during the filtration process are expected to be obtained by 3D tomography, playing a critical role in determining the predominant capture mechanism of the filters.

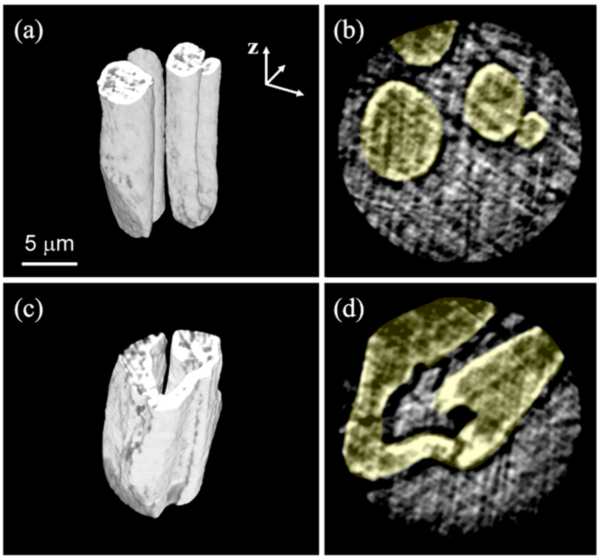

Figure 6. 3D TXM reconstructed image and the slice plane along *z*-direction of the N95 mask in (**a**) and (**b**); those of the 3M filter in (**c**) and (**d**), respectively.

5. Conclusions

The fiber diameter and porosity strongly affect filtration performance. Despite being made of the same fiber material, the N95 mask reveals a higher collection efficiency while the 3M air filter exhibits a lower pressure drop. To satisfy the vital demand on the specific aspects of fibrous filtration, the priority of air filter media is given towards higher collection efficiency or lower pressure drop. For the design of the filter to effectively capture the ultrafine particles, smaller fiber diameter, stronger surface charge, and optimal porosity should be involved. Our findings demonstrate the promising capabilities of 3D TXM tomography in determining the porosity of fibrous filter as well as in proposing practical filtration models of real geometrical arrangements of fiber–fiber and fiber–particle for further simulation studies. The simulated results of the deposition of NaCl aerosols on the real geometry of fibrous filters will be persuasive in providing great insight into fundamental breakthrough and primary parameters governing the filtration mechanism.

Author Contributions: Conceptualization, E.W.H.; software, C.-H.W.; formal analysis, T.-N.L., C.-Y.M. and Y-L.H.; investigation, C.-Y.M.; resources, S.-H.H., W.-C.K. and C.-C.W.; writing—original draft preparation, T.-N.L.; writing—review and editing, C.-C.W. and E.W.H.; supervision, E.W.H.; project administration, E.W.H.

Funding: The authors are grateful to the support of the Ministry of Science and Technology (MOST) Programs MOST-108-3017-F-009-003, 107-2218-E-007-012, 107-3017-F-009-002, 107-3017-F-007-003, 107-3017-F-009-002, 107-3011-F-002-002, 104-2628-E-009-003-MY3, 106-2811-E-009-032, 106-2218-E-007-019, 106-2514-S-007-004, 106-3011-F-002-002, and 108-2221-E-009-131-MY4. This work was financially supported by the "Center for the Semiconductor Technology Research" from The Featured Areas Research Center Program within the framework of the Higher Education Sprout Project by the Ministry of Education (MOE) in Taiwan. Also supported in part by the MOST, Taiwan, under Grant MOST-108-3017-F-009-003. EWH and TNL are supported by MOST 107-2628-E-009-001-MY3.

Acknowledgments: We especially thank Yu-Hsiang Hsu of the National Taiwan University (NTU) for sample preparations, Chih-Chieh Chen of the NTU for filtration test, and Yao-Hsien Liu of the National Chiao Tung University for simulation. Our sincere thanks go to Yen-Fang Song, who is the BL01B1 team of the National Synchrotron Radiation Research Center (NSRRC) Experimental Facility Division. We greatly appreciate the beam time and help from the NSRRC.

Conflicts of Interest: The authors declare no conflict of interest.

References

1. Jalava, P.I.; Happo, M.S.; Huttunen, K.; Sillanpaa, M.; Hillamo, R.; Salonen, R.O.; Hirvonen, M.R. Chemical and microbial components of urban air PM cause seasonal variation of toxicological activity. *Environ. Toxicol Pharm.* **2015**, *40*, 375–387. [CrossRef] [PubMed]
2. Rajak, A. Synthesis of Electrospun Nanofibers Membrane and Its Optimization for Aerosol Filter Application. *KnE Eng.* **2016**, *1*. [CrossRef]
3. Zhu, M.; Han, J.; Wang, F.; Shao, W.; Xiong, R.; Zhang, Q.; Pan, H.; Yang, Y.; Samal, S.K.; Zhang, F.; et al. Electrospun Nanofibers Membranes for Effective Air Filtration. *Macromol. Mater. Eng.* **2017**, *302*, 1600353. [CrossRef]
4. Li, P.; Wang, C.; Zhang, Y.; Wei, F. Air filtration in the free molecular flow regime: A review of high-efficiency particulate air filters based on carbon nanotubes. *Small* **2014**, *10*, 4543–4561. [CrossRef] [PubMed]
5. Chen, C.C.; Huang, S.H. The effects of particle charge on the performance of a filtering facepiece. *Am. Ind Hyg. Assoc. J.* **1998**, *59*, 227–233. [CrossRef]
6. Yang, C. Aerosol Filtration Application Using Fibrous Media—An Industrial Perspective. *Chin. J. Chem. Eng.* **2012**, *20*, 1–9. [CrossRef]
7. Romay, F.J.; Liu, B.Y.H.; Chae, S.-J. Experimental Study of Electrostatic Capture Mechanisms in Commercial Electret Filters. *Aerosol Sci. Technol.* **1998**, *28*, 224–234. [CrossRef]
8. Huang, S.-H.; Chen, C.-W.; Chang, C.-P.; Lai, C.-Y.; Chen, C.-C. Penetration of 4.5nm to aerosol particles through fibrous filters. *J. Aerosol Sci.* **2007**, *38*, 719–727. [CrossRef]
9. Wang, C.-S. Electrostatic forces in fibrous filters—A review. *Powder Technol.* **2001**, *118*, 166. [CrossRef]
10. Zhou, Y.; Cheng, Y.S. Evaluation of N95 Filtering Facepiece Respirators Challenged with Engineered Nanoparticles. *Aerosol Air Qual. Res.* **2017**, *16*, 212–220. [CrossRef]
11. Mostofi, R.; Wang, B.; Haghighat, F.; Bahloul, A.; Jaime, L. Performance of mechanical filters and respirators for capturing nanoparticles-limitations and future direction. *Ind. Health* **2010**, *48*, 296–304. [CrossRef] [PubMed]
12. Gervais, P.C.; Bémer, D.; Bourrous, S.; Ricciardi, L. Airflow and particle transport simulations for predicting permeability and aerosol filtration efficiency in fibrous media. *Chem. Eng. Sci.* **2017**, *165*, 154–164. [CrossRef]
13. Sambaer, W.; Zatloukal, M.; Kimmer, D. 3D modeling of filtration process via polyurethane nanofiber based nonwoven filters prepared by electrospinning process. *Chem. Eng. Sci.* **2011**, *66*, 613–623. [CrossRef]
14. Soltani, P.; Zarrebini, M.; Laghaei, R.; Hassanpour, A. Prediction of permeability of realistic and virtual layered nonwovens using combined application of X-ray µ CT and computer simulation. *Chem. Eng. Res. Des.* **2017**, *124*, 299–312. [CrossRef]
15. Gervais, P.C.; Bourrous, S.; Dany, F.; Bouilloux, L.; Ricciardi, L. Simulations of filter media performances from microtomography-based computational domain. Experimental and analytical comparison. *Comput. Fluids* **2015**, *116*, 118–128. [CrossRef]

16. Martin, S.B., Jr.; Moyer, E.S. Electrostatic respirator filter media: Filter efficiency and most penetrating particle size effects. *Appl. Occup. Environ. Hyg.* **2000**, *15*, 609–617. [CrossRef]
17. Rother, C.; Kolmogorov, V.; Blake, A. GrabCut Interactive foreground extraction using iterated graph cuts. *ACM Trans. Graph.* **2004**, *23*, 309–314.
18. Martin, W.D.; Putman, B.J.; Kaye, N.B. Using image analysis to measure the porosity distribution of a porous pavement. *Constr. Build. Mater.* **2013**, *48*, 210–217. [CrossRef]
19. Tsai, P.-I.; Lam, T.-N.; Wu, M.-H.; Tseng, K.-Y.; Chang, Y.-W.; Sun, J.-S.; Li, Y.-Y.; Lee, M.-H.; Chen, S.-Y.; Chang, C.-K.; et al. Multi-scale mapping for collagen-regulated mineralization in bone remodeling of additive manufacturing porous implants. *Mater. Chem. Phys.* **2019**, *230*, 83–92. [CrossRef]
20. Lam, T.N.; Huang, W.J.; Wang, C.C.; Chuang, W.T.; Su, Y.W.; Huang, E.W. Micro-Layer and Lattice Structure Effects on Impedance of Titanium Oxide Phthalocyanine. *Adv. Eng. Mater.* **2018**, 1–5. [CrossRef]
21. Wang, C.C.; Chiang, C.C.; Liang, B.; Yin, G.C.; Weng, Y.T.; Wang, L.C. Fast Projection Matching for X-ray Tomography. *Sci. Rep.* **2017**, *7*, 3691. [CrossRef] [PubMed]
22. Parkinson, D.Y.; Knoechel, C.; Yang, C.; Larabell, C.A.; Le Gros, M.A. Automatic alignment and reconstruction of images for soft X-ray tomography. *J. Struct. Biol.* **2012**, *177*, 259–266. [CrossRef] [PubMed]
23. Wang, Y.; Pu, J.; Wang, L.; Wang, J.; Jiang, Z.; Song, Y.-F.; Wang, C.-C.; Wang, Y.; Jin, C. Characterization of typical 3D pore networks of Jiulaodong formation shale using nano-transmission X-ray microscopy. *Fuel* **2016**, *170*, 84–91. [CrossRef]
24. Xue, J. Face Masks Having an Elastic and Polyolefin Thermoplastic Band Attached Thereto by Heat and Pressure. U.S. Patent US 6332465B1, 14 December 2000.
25. John, M.; Brandner, W.J.K.; Seyed, A.; Angadjivand, J.; Springett, E.; Timothy, J. Lindquist Monocomponent Monolayer Meltblown Web and Meltblowing Apparatus. U.S. Patent US 7902096 B2, 8 March 2011.
26. Humlicek, L.D. Pillowed Web of Blown Microfibers. U.S. Patent US 4103058A, 25 July 1978.
27. Leung, W.W.-F.; Hung, C.-H.; Yuen, P.-T. Effect of face velocity, nanofiber packing density and thickness on filtration performance of filters with nanofibers coated on a substrate. *Sep. Purif. Technol.* **2010**, *71*, 30–37. [CrossRef]
28. Zhang, S.; Shim, W.S.; Kim, J. Design of ultra-fine nonwovens via electrospinning of Nylon 6: Spinning parameters and filtration efficiency. *Mater. Des.* **2009**, *30*, 3659–3666. [CrossRef]
29. Lee, K.W.; Liu, B.Y.H. On the Minimum Efficiency and the Most Penetrating Particle Size for Fibrous Filters. *J. Air Pollut. Control. Assoc.* **1980**, *30*, 377–381. [CrossRef]
30. Ahn, Y.C.; Park, S.K.; Kim, G.T.; Hwang, Y.J.; Lee, C.G.; Shin, H.S.; Lee, J.K. Development of high efficiency nanofilters made of nanofibers. *Curr. Appl. Phys.* **2006**, *6*, 1030–1035. [CrossRef]
31. Kulkarni, P.; Baron, P.A.; Willeke, K. *Aerosol Measurement: Principles, Techniques, and Applications*; John Wiley Sons: Hoboken, NJ, USA, 2011.
32. Brown, R.C. *Air Filtration: An Integrated Approach to the Theory and Applications of Fibrous Filters*; Pergamon Press: Oxford, NY, USA, 1993.
33. Hinds, W.C. *Aerosol Technology: Properties, Behavior, and Measurement of Airborne Particles*; John Wiley Sons: Hoboken, NJ, USA, 1999.